On the effect of thin-wall thickness on melt pool dimensions in laser powder-bed fusion of Hastelloy X: Numerical modeling and experimental validation

Shahriar Imani Shahabad [a],[*], Usman Ali [b], Zhidong Zhang [a], Ali Keshavarzkermani [a], Reza Esmaeilizadeh [a], Ali Bonakdar [c], Ehsan Toyserkani [a]

[a] Department of Mechanical and Mechatronics Engineering, University of Waterloo, 200 University Avenue West, Waterloo, Ontario N2L 3G1, Canada
[b] Mechanical Engineering Department, King Fahd University of Petroleum & Minerals, Dhahran 31261, Saudi Arabia
[c] Siemens Energy Canada Limited, 9505 Côte-de-Liesse, Montréal, Québec H9P 1A5, Canada

ARTICLE INFO

ABSTRACT

Laser Powder-bed Fusion (LPBF) is a common technique categorized as one of the Additive Manufacturing (AM) processes to efficiently fabricate complex geometries. The involvement of complex phenomena relating to laser and metal powder requires a thorough investigation to understand the complex multi-physics behind this process. Modeling and simulation tools shed light on predicting the temperature distribution and melt pool dimensions which have a significant impact on the quality of the final parts. In this study, a three-dimensional (3D) heat transfer model is developed to investigate the influence of the thickness of the printed thin-walls on melt pool dimensions and temperature distribution. The results indicate that the single-track simulation can predict the melt pool dimensions accurately and the calibrated model can be extended to the multi-track simulation for investigating the effect of thin-wall thicknesses on melt pool geometries. The simulation results demonstrate the evolution of melt pool geometries during the process. Due to the existence of heat accumulation during the process, decreasing the thicknesses of the thin-walls leads to enlarging the melt pool width significantly. Moreover, the simulation results show a higher temperature gradient during the LPBF process of thinner parts leading to a smaller grain size of the final microstructure. The validation of the simulation results showed the high capability of the model in predicting the transient temperature profile and melt pool geometries. The percentage difference between simulated and experimental melt pool width for thin-wall thicknesses 0.5 mm, 0.75 mm, and 1 mm are 7%, 7%, and 11%, respectively. Lastly, a process map has been provided to guide the selection of process parameters for printing thin-wall structures.

1. Introduction

Laser Powder-bed Fusion (LPBF) is one of the most common types of Additive Manufacturing (AM) processes for producing intricate geometries in a layer-by-layer fashion [1]. As it is observed in Fig. 1, the powder layer is spread by the recoater on top of the build station and the laser heat source scans the powder material. In the next step, the building platform moves downward and the powder delivery system moves upward to spread another layer on top of the previous scanned layer. The process of melting and solidification of the powder material layer-by-layer continues until the final part is printed [2,3]. In recent years, LPBF has gained significant attraction in various industries and is being used for producing complex geometries at comparable costs to conventional manufacturing techniques [4]. One of the biggest challenges in manufacturing parts with desirable properties is the use of appropriate process parameters. It is important to use the correct process parameters as they have a significant influence on the quality of final parts [5,6]. As the LPBF process consists of a large number (~100) of parameters (e.g. laser power, scanning speed, hatch distance, layer thickness, etc.), it is important to understand the effect of process parameters on part performance [7].

The melt pool formation and solidification during laser scanning of the powder material are one of the most studied topics in LPBF as it directly affects the part density [8], microstructure [9], and strength of the printed parts [10]. In addition, the input process parameters have a

Nomenclature

C_p	Specific heat
I	Heat intensity distribution
$Q(x, y, z, t)$	Internal heat generation per unit volume
k	Thermal conductivity
r_d	The lower radius of the heat source
q_c	Convective heat dissipation
σ_{sb}	Stefan-Boltzmann coefficient
z_e	z coordinates of the upper surface of the heat source
h_c	Convection heat transfer coefficient
H	Heat source height
q_0	The highest amount of heat intensity
ε	Emissivity coefficient
r_0	The upper radius of the heat source
α	Absorption coefficient
L	Latent heat
P	Laser power
q_r	Radiative heat dissipation
V	Scanning speed
ρ	Density
z_i	z coordinates of the lower surface of the heat source
k_e	Effective thermal conductivity of powder material
k_s	Thermal conductivity of solid material

k_R	Thermal conductivity of the powder bed related to the radiation
$k_{contact}$	Thermal conductivity attributed to the contact area of the particles
k_g	The surrounding gas thermal conductivity
B	Particle deformation parameter
$\varnothing$	The surface area of the particle in contact with another particle
φ	The porosity of the powder bed
$\dot{T}$	Cooling rate
G	Temperature gradient
R	Solidification rate
$T_{base}(x, y, z)$	The temperature of the bottom surface
T_0	Ambient temperature
$\boldsymbol{R_Q}$	Internal heat vector
$\boldsymbol{K}$	Conduction matrix
$\boldsymbol{M}$	Capacitance matrix
$\boldsymbol{R_c}$	Convection vector
$\boldsymbol{R_r}$	Radiation vector
$\boldsymbol{N}$	Matrix of shape functions
$\widehat{\boldsymbol{T}}$	Temperature vector of an element
$\boldsymbol{B}$	Differential temperature matrix

significant effect on the melt pool shape [11]. Keshavarzkermani et al. [12] studied the effect of laser energy density (LED) on melt pool geometry and found out that finer cell structure in the melt pool was obtained by higher laser power. Staub et al. [13] investigated the effect of using high laser power on the induced residual stress. Their results showed that larger and flatter melt pool dimensions provide higher residual stress in printed parts. Moreover, Criales et al. [14] studied the effect of process parameters on melt pool shapes and dimensions and found variations in the melt pool geometry along the laser track. The importance of process parameters on melt pool behavior was statistically analyzed by Kamath [15] and it was concluded that scan speed was the most significant parameter.

The time and cost of experimental investigations into the effect of input process parameters on melt pool geometries have driven the
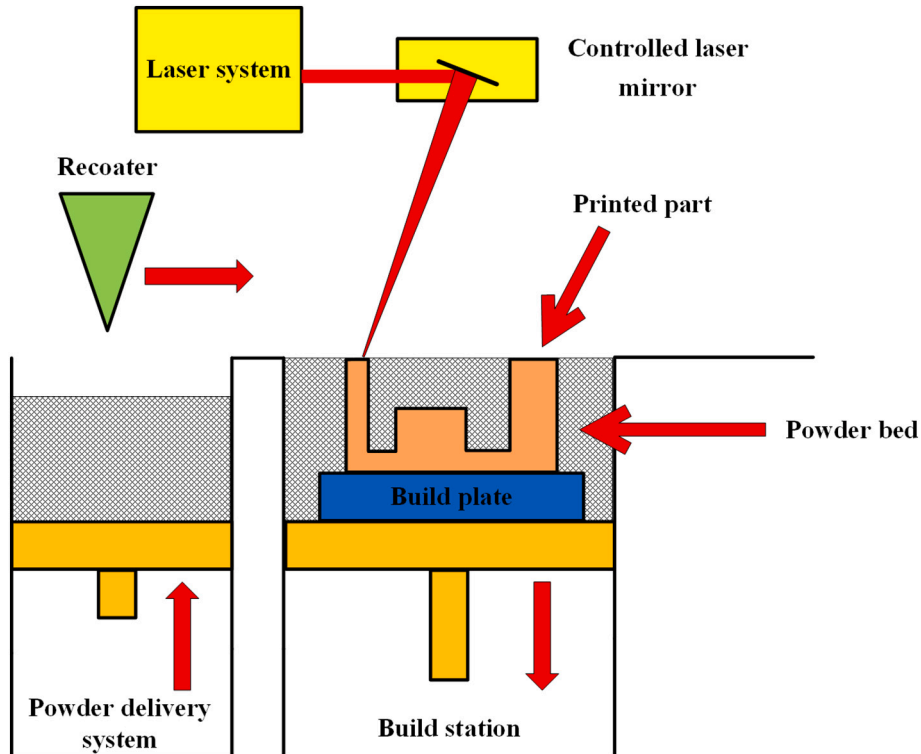

Fig. 1. Schematic of the laser powder-bed fusion (LPBF) process.

motivation of researchers to study the influence of process parameters by modeling and simulation [16]. Therefore, a detailed model is required to study the effect of input process parameters for conducting process optimization leading to high-quality parts [17]. Numerical modeling techniques such as Finite Element (FE) analysis provide an effective approach for predicting the influence of input process parameters on melt pool characteristics and transient temperature during the process [18]. Yuan et al. [19] investigated the laser scanning speed influence on melt pool formations and categorized different regions of scanning speed based on the stability of melt pool formation. Shahabad et al. [20] studied the effect of process parameters (laser power and speed) on melt pool dimensions and concluded that laser power had a dominant effect on the melt pool geometries. Li et al. [21] studied the effect of laser power and scanning speed on melt pool dimensions and found that the width, depth, and length of the molten region had a proportional relationship with laser power. Zhang et al. [22] conducted a comprehensive study on various heat source models for predicting melt pool shape. The effect of process parameters (laser power and scanning speed) was studied, and they proposed and validated a novel heat source for predicting accurate melt pool shape. Moreover, Loh et al. [23] investigated the effect of laser beam distribution on the melt pool dimensions. They found that uniform and Gaussian distribution provided the same melt pool depth but different widths. Although comprehensive investigations have been conducted on the effect of process parameters on melt pool shapes, however, very few studies have been carried out on the influence of part's geometry on melt pool shapes and dimensions.

In addition to the laser process parameters, the geometry of the part plays a critical role in the melt pool dimensions, formed microstructure, and mechanical behavior of printed parts. Leicht et al. [24] studied the effect of rib thickness and build angles on the microstructure of 316L parts. They concluded that 0.4 mm and 45° build angles as critical thickness and build angle for avoiding large elongated grains. Similarly, Liang et al. [25] found that smaller geometric sizes (less than 1 mm) resulted in poor cooling conditions and affected the elastic modulus and hardness. Piazza et al. [26] conducted research on the influence of part geometry on melt pool dimensions and the hardness of printed parts of 316L stainless steel material. They investigated two different geometries including cylindrical and conical shapes. They observed that due to the existence of heat accumulation, the melt pool depth became shallower with the increase in height of the cylindrical geometry.

There is a lack of research on the effect of part geometry on melt pool dimensions and to the best knowledge of the authors, this is the first work that investigates the effect of thin-wall thickness on melt pool shapes and dimensions experimentally and numerically. To this end, a high fidelity numerical model to predict the influences of input process parameters and part geometries on the melt pool dimensions was

developed. Hastelloy X thin-walls were printed with different thicknesses to assess the influence of part geometries on melt pool shapes and microstructures experimentally. The results show the effect of melt pool evolution leading to the melt pool stability and the geometry dependency in a multi-track LPBF process. Therefore, a decrease in the thicknesses of the thin-walls results in increasing the melt pool width substantially due to the heat accumulation happening during the process. Moreover, the results show that a higher temperature gradient induced during the LPBF process of thinner parts resulting in smaller grain sizes of the final microstructure. Lastly, the process map is developed which is a guide for choosing the proper range of process parameters based on the dimensions of the thin-wall thicknesses for printing the high-quality parts.

2. Materials and methods

To investigate the influence of part geometry on melt pool shapes, three thin-walls of different thicknesses (0.5 mm, 0.75 mm, 1 mm) with three repetitions were printed as shown in Fig. 2. EOS M290 machine (EOS GmbH, Krailling, Germany) printed all samples using stripe scanning strategy without any rotation on each layer with a laser power of 200 W, scanning speed of 1000 mm/s, hatch distance of 90 μm, and layer thickness of 40 μm. Hastelloy X powder was selected for this study with a size distribution of D10 < 15.5 μm, D50 < 29.3 μm, and D90 < 46.4 μm [27].

Table 1 shows the chemical composition of the Hastelloy X powder used in the current investigation. To analyze the morphology of the powder distribution, Zeiss Ultra Plus (Carl Zeiss Microscopy GmbH, Jena, Germany) Scanning Electron Microscopy (SEM) was used (Fig. 3). Besides, for capturing the grain size and Electron Backscatter Diffraction (EBSD) images, VEGA3 (Tescan Orsay Holding, Kohoutovice, Czech Republic) SEM was utilized.

SiC grinding papers were used to polish the samples manually (from 320 to 4000 grit sizes). The final polishing step was done with 0.05 μm alumina slurry and colloidal silica suspension using Buehler VIBROMET 2 vibratory polisher (Buehler, Leinfelden-Echterdingen, Germany) and rinsed with ethanol to remove residual alumina/colloidal silica from the samples' surface. Glyceregia (HCl 50 ml, HNO3 10 ml, Glycerol 10 ml) was used for etching and melt pools observation where samples were held in the Glyceregia etchant for about 1 min. The resulting melt pool geometries were obtained using a Keyence VK-X250 confocal laser microscope (Keyence Corporation, Osaka, Japan).

3. Finite element (FE) modeling

Finite Element (FE) analysis was conducted to investigate the effect of part geometries on temperature distribution and melt pool evolution
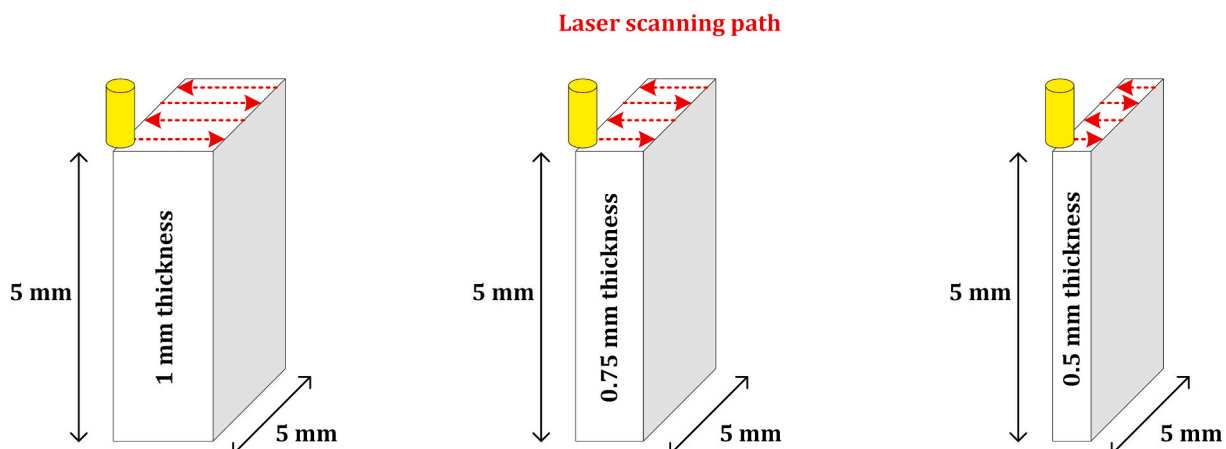
Laser scanning path

Fig. 2. Geometry dimensions of thin-walls.

Table 1

Hastelloy X powder chemical composition (in wt%) [28].

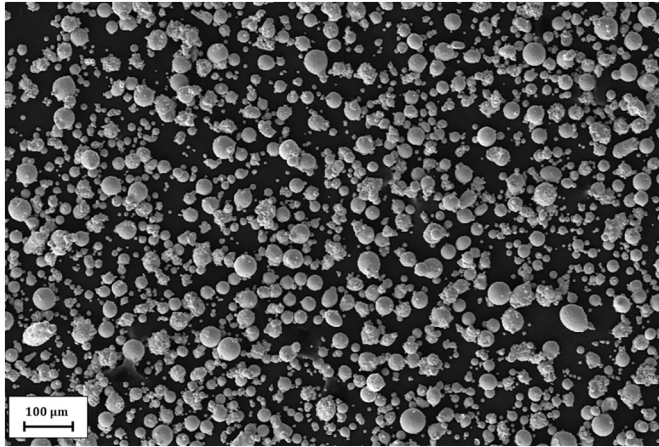| C	Si	Cr	Mn	W	Ti	Cu	Fe	Mo	Co	Al	Ni
<0.1	<1	21.75 ± 1.25	<1	0.6 ± 0.4	<0.15	<0.5	18.5 ± 1.5	9 ± 1	1.5 ± 1	<0.5	balance

Fig. 3. Powder distribution of Hastelloy X [20].

during the LPBF process. A three-dimensional transient thermal model was developed using commercial software COMSOL Multiphysics®. Irreversible phase change transformation, anisotropic thermal conductivity, and volumetric heat source were considered to provide a more accurate prediction of temperature profile and melt pool geometries during the process. The advantages of using anisotropic thermal conductivity and volumetric heat source have been outlined in a previous work by the authors [22]. The procedure of developing the FE model is described in the following sections.

3.1. Model geometry

Two different LPBF models were developed for the (a) single-track and (b) multi-track simulations as shown in Fig. 4. The smaller domain size (1 mm × 0.5 mm × 0.5 mm) with half symmetry was used for capturing the melt pool and calibration of the heat source model in the single-track simulation process. On the other hand, thin-walls with the same geometry as printed parts (5 × 5 × 0.5 mm, 5 × 5 × 0.75 mm, and 5 × 5 × 1 mm) were modeled for simulating the multi-track LPBF process. Calibrated and validated parameters from the single-track simulations were used to model and validate the multi-track simulations.

Fig. 4a–b demonstrates the schematic of model geometry of the single-track and the multi-track process for the thin-wall thickness of 1 mm. The top layer shows the powder layer with a thickness of 40 μm as a continuous domain. A uniform cuboid mesh was created for both models in the domain with a maximum element size of 20 μm. The number of elements used for the single-track modeling was 7395, while 25,500 elements were implemented in the multi-track process of the thin-wall thickness of 1 mm. The small time step of 5 μs is chosen in the modeling for capturing the high speed of laser movement.

3.2. Material properties

3.2.1. Thermal conductivity

One of the most crucial physical properties required for conducting thermal analysis is the thermal conductivity of the powder and bulk material. It is realized that the thermal conductivity of the bulk and powder material is extremely different from each other. Sih and Barlow [29] derived a relationship considering the powder compaction factor, particle shapes, and other parameters related to the powder layer which has a significant effect on the thermal conductivity, (Eq. (1)).
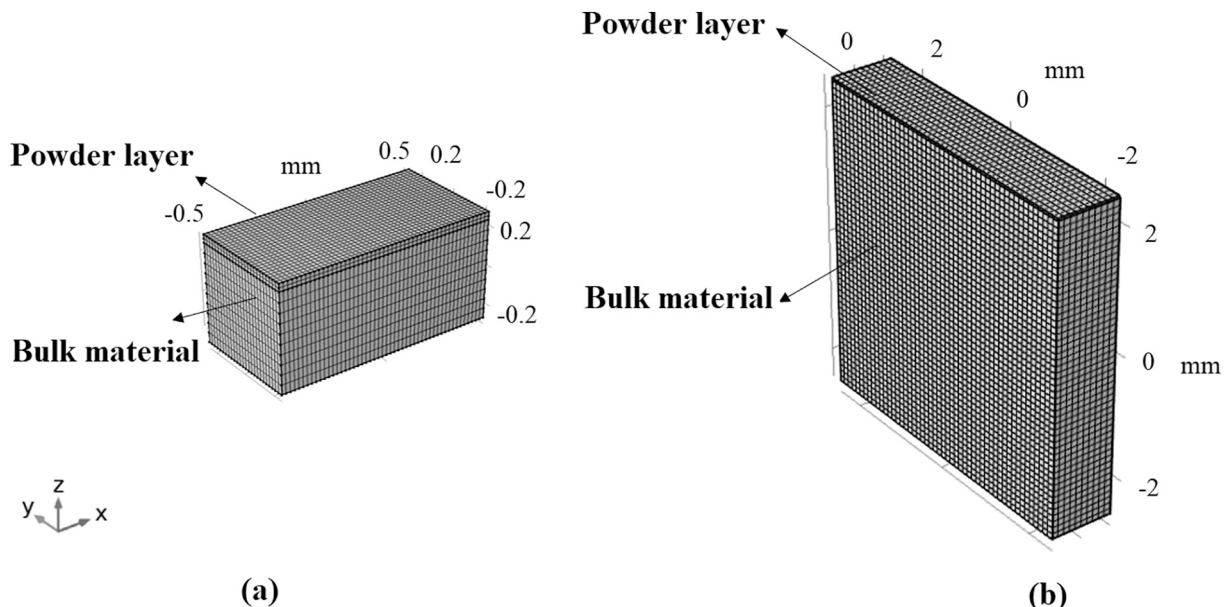

Fig. 4. Meshed geometry model, a) single-track model, b) example of the multi-track model.

$$\frac{k_e}{k_g} = \left(1 - \sqrt{1-\varphi}\right)\left(1 + \frac{\varphi k_R}{k_g}\right) + \sqrt{1-\varphi}\left\{(1-\varnothing)\left[\frac{2}{1-\frac{Bk_g}{k_s}}\left(\frac{B}{\left(1-\frac{Bk_g}{k_s}\right)^2}\left(1-\frac{k_g}{k_s}\right)Ln\frac{k_s}{Bk_g} - \frac{B+1}{2} - \frac{B-1}{1-\frac{Bk_g}{k_s}}\right) + \frac{k_R}{k_g}\right] + \varnothing\frac{k_{\text{Contact}}}{k_g}\right\} \tag{1}$$

where k_e is the effective thermal conductivity of powder material, k_g is the thermal conductivity of the argon gas, k_R is the thermal conductivity of the powder bed related to radiation, k_s is the thermal conductivity of solid material, φ is related to the porosity of the powder bed (52%) [30], $\varnothing$ is the surface contact area of particles which is set to be 3×10^{-4}, B is deformation parameter of the particle equals to 1, and k_{contact} can be derived from Eq. (2) [29].

$$\left\{\begin{array}{ll} k_{\text{contact}} = 18\varnothing k_s & \varnothing \leq 3 \times 10^{-4} \\ k_{\text{contact}} \approx k_s & \varnothing > 0.01 \end{array}\right\} \tag{2}$$

The thermal conductivity of the powder material versus bulk material is shown in Fig. 5. It is realized that the thermal conductivity of the powder material is extremely small compared to the bulk material and above melting temperature (1581 K), the thermal conductivity of the powder will be increased significantly due to the phase change [20].

3.2.2. Specific heat capacity

The latent heat of fusion plays a crucial role in defining the specific heat capacity of the material. In other words, the phase transformation from powder to liquid requires heat absorption for overcoming the heat capacity of the material and is called the latent heat of fusion. The apparent heat capacity method is utilized for considering the latent heat of fusion during the melting process as shown in Eq. (3) [31].

$$C_p = \left\{\begin{array}{l} C_{p,sensible} \quad \text{if } T < T_m - 0.5\Delta T_m \ \text{ or } \ T > T_m + 0.5\Delta T_m \\ C_{p,modified} = C_{p,sensible} + \frac{L}{\Delta T_m} \ \text{ if } T_m - 0.5\Delta T_m < T < T_m + 0.5\Delta T_m \end{array}\right\} \tag{3}$$

where $C_{p,\,sensible}$ is the original specific heat capacity of the material for the temperature range beyond solidus and liquidus whereas $C_{p,\,modified}$ is the adjusted specific heat capacity of the material when the phase change occurs. T_m is the average temperature of solidus and liquids temperatures (1581 K), L (227 KJ/Kg) is the latent heat of fusion of the
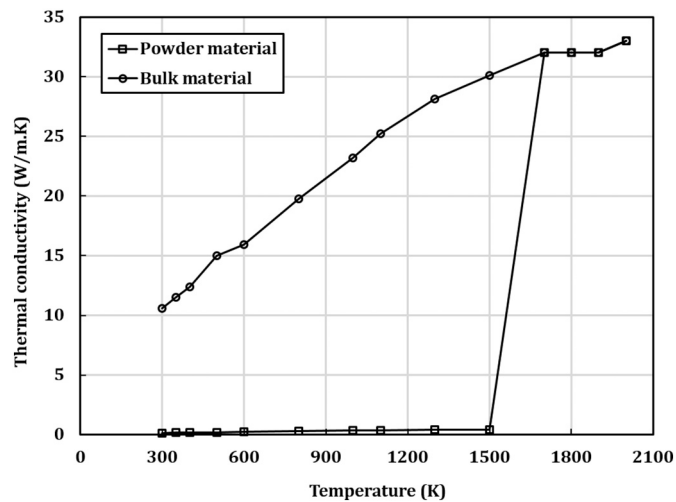
material and ΔT_m is the difference between liquidus (1628 K) and solidus temperature (1533 K). As can be seen in Fig. 6, specific heat capacity rises drastically to compensate for heat absorption of latent heat fusion during phase transformation.

3.2.3. Density

Powder-bed compaction density is acquired experimentally as described in [30]. By considering the powder compaction and the existence of porosities between particles, the density of the powder layer is obtained from Eq. (4). Fig. 7 demonstrates the difference of temperature-dependent density between powder versus bulk material [20].
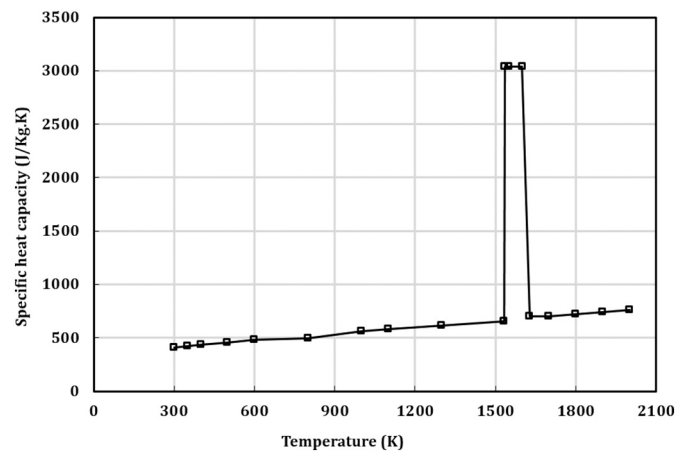
$$\rho_{\text{powder}} = (1-\varphi)\rho_{\text{bulk}} \tag{4}$$

Fig. 6. Temperature-dependent specific heat of the material.

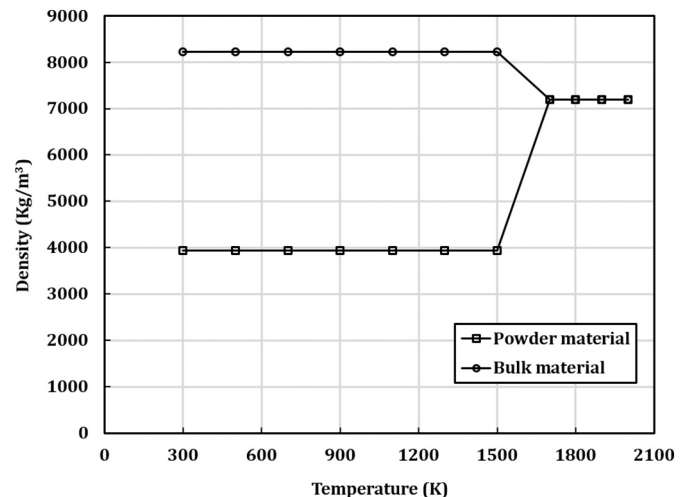**Fig. 5.** Temperature-dependent thermal conductivity of the material.

Fig. 7. The temperature-dependent density of the material.

3.3. Heat transfer governing equation and boundary conditions

The governing equation of heat transfer (Fourier's law) can be described as [11]:

$$\rho C_p \frac{\partial T}{\partial t} = \frac{\partial}{\partial x}\left(k_x \frac{\partial T}{\partial x}\right) + \frac{\partial}{\partial y}\left(k_y \frac{\partial T}{\partial y}\right) + \frac{\partial}{\partial z}\left(k_z \frac{\partial T}{\partial z}\right) + Q\,(x, y, z, t) \quad (5)$$

where k_x, k_y, k_z, C_p, T, ρ, and Q are thermal conductivity [W/mK] in different coordinate directions x, y, and z, specific heat [J/kgK], temperature [K], the material's density [kg/m^3], and internal heat generation per unit volume [W/m^3], respectively. The internal heat generation per volume is considered as the heat source model in the LPBF process. The initial temperature of the whole part is assumed to be the ambient temperature of 293 K except the bottom surface of the part (Γ_1) which is preheated and offset at 373 K. It is realized that due to local heating induced by the laser and its high speed, the build-up temperature from previous layers would not have a significant effect on melt pool dimensions. Besides, the delay time interval between the scanning of each layer (12 s) would provide enough time for cooling the part significantly close to ambient temperature. However, after scanning multiple layers, there would be a slight increase in the temperature eventually. Further information regarding the initial boundary condition is demonstrated in Fig. S.1 of supplementary material.

$$T_{base}(x, y, z) = 373\,K \text{ on } \Gamma_1 \quad (6)$$

To compensate for the effect of fluid convective heat transfer, anisotropic enhanced thermal conductivity is considered based on Eq. (7) [32,33].

$$k_x = \lambda_x k, \quad k_y = \lambda_y k, \quad k_z = \lambda_z k$$
$$\begin{cases} \lambda_x = \lambda_y = \lambda_z = 1, \ \ T < T_{melting} \\ \lambda_x = 1, \ \ \lambda_y = 4 \quad \lambda_z = 20 \quad T \geq T_{melting} \end{cases} \quad (7)$$

It should be noted that the enhancement factors can be identified based on the experimental results.

Based on Newton's law (Eq. (8)), a convective heat transfer to the surrounding area was considered on the top domain surface (Γ_2).

$$q_c = -h_c(T - T_0) \text{ on } \Gamma_2 \quad (8)$$

where q_c is convective heat transfer, T_0 is the ambient temperature (293 K), h_c is the convection heat transfer coefficient [W/m^{2}K], and T is the temperature of the part.

Besides, a radiative heat transfer of the upper domain surface (Γ_3) to the ambient was taken into the account based on (Eq. (9)).

$$q_r = -\sigma_{sb}\varepsilon\left(T^4 - T_0^4\right) \text{ on } \Gamma_3 \quad (9)$$

where, σ_{sb} are the Stefan-Boltzmann coefficient [W/m^{2}K^4] and ε is the emissivity coefficient.

It should be noted that the sides of the thin-walls are considered as isolated boundary conditions since the thermal conductivity of the powder is much less compared to the bulk material (approximately 1% of bulk material). Therefore, the heat transfer between the bulk and surrounded powder on the sides of the part is negligible.

After using the Galerkin method on Eq. (5) and discretizing its weak form in space and time, the heat transfer system equations will be generated in Eq. (10). The backward Euler time-stepping method is implemented in COMSOL Multiphysics® software.

$$M \frac{\left(^{t+\Delta t}\widehat{T} - {}^t\widehat{T}\right)}{\Delta t} + {}^{t+\Delta t}(K\widehat{T}) = {}^{t+\Delta t}(R_Q + R_c + R_r) \quad (10)$$

In this equation, M is the capacitance matrix, $\widehat{T}$ is the temperature vector of an element, and K is the conduction matrix. R_Q is the internal heat vector. R_c and R_r are boundary condition vectors for convection and radiation, respectively. The expressions are shown as follows,

$$M = \sum_e \int_{\Omega_e} \rho_e c_e N^T N d\Omega$$
$$K = \sum_e \int_{\Omega_e} B^T k_e B d\Omega$$
$$R_Q = \sum_e \int_{\Omega_{e_Q}} N^T Q(x, y, z, t) d\Omega \quad (11)$$
$$R_c = \sum_e \int_{\Gamma_{e_2}} -h_c N^T (N\widehat{T} - T_0) d\Gamma$$
$$R_r = \sum_e \int_{\Gamma_{e_3}} -\varepsilon\sigma N^T \left((N\widehat{T})^{\circ 4} - T_0^{\circ 4}\right) d\Gamma$$

where N is a matrix of shape functions of an element with n node, and the differential matrix is expressed as B. Besides, $\circ$ is the element-wise power operation.

3.4. Volumetric heat source model

To predict the melt pool dimensions and temperature distribution during the process a three-dimensional (3D) conical-Gaussian heat source model was used (Fig. 8).

The conical-Gaussian heat source is formulated in given as (Eq. (12)) [22]:
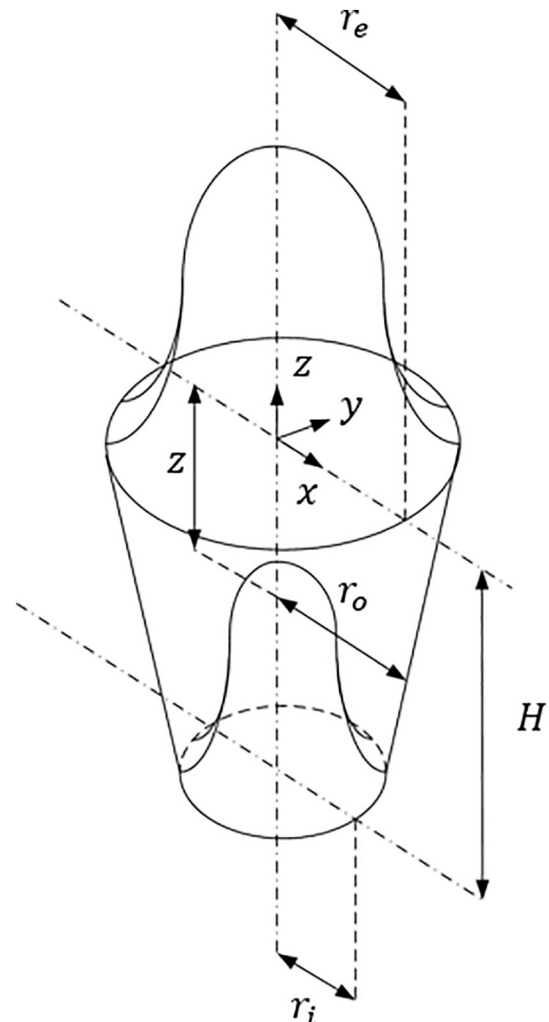

Fig. 8. Conical-Gaussian volumetric heat source [34].

$$I(x, y, z) = q_0 . exp\left(-2\frac{x^2 + y^2}{r_0^2}\right) \quad (12)$$

$$\boldsymbol{r_0}(z) = \boldsymbol{r_e} + \frac{\boldsymbol{z}}{\boldsymbol{H}}(\boldsymbol{r_e} - \boldsymbol{r_i}) \quad (13)$$

where q_0, r_e, r_i and $I(x,y,z)$, are the highest amount of heat intensity, the upper and lower radius of the heat source, and heat intensity distribution, respectively. The volumetric heat source has a Gaussian profile shape while the heat flux input penetration decays linearly in the z-direction.

Eq. (14) can be described as follows according to the thermal energy conservation:

$$\alpha.P = \int_{-H}^{0} \int_{-\infty}^{\infty} \int_{-\infty}^{\infty} q_0 . exp\left(-2\frac{x^2 + y^2}{r_0^2}\right) dx dy dz \quad (14)$$

where P and α are laser power and laser irradiation absorptivity, respectively.

By solving this equation, q_0 can be calculated from Eq. (15):

$$q_0 = \frac{6\alpha \cdot P}{\pi H \left(r_e^2 + r_e r_i + r_i^2\right)} \quad (15)$$

In this equation, H is the height of the heat source model.

Finally, the equation of heat intensity distribution of the heat source model (Eq. (16)) can be achieved by substituting q_0 in Eq. (12).

$$I(x, y, z) = \frac{6\alpha.P}{\pi H \left(r_e^2 + r_e r_i + r_i^2\right)} . exp\left(-2\frac{x^2 + y^2}{r_0^2}\right) \quad (16)$$

4. Results and discussion

In this section, the experimental and simulation results are presented. Single-track and multi-track simulations are developed for predicting the melt pool dimensions. The effect of part geometry (thin-wall thickness) on the transient temperature profile, temperature gradient, and melt pool dimensions are investigated numerically and experimentally. Finally, the process map is developed for printing high-quality parts.

4.1. Experimental measurements

The melt pool dimensions (melt pool depth and width) were measured using a confocal laser microscope. In the single-track and multi-track processes, three repetitions for each set of process parameters have been considered. By measuring the melt pool dimensions and averaging the values the data point from experimental work can be achieved.

Fig. 9 illustrates the melt pool shapes based on different sample thicknesses. The thickness of thin-walls significantly influenced the shape and dimensions of the melt pool. Results show that decreasing the thickness causes the melt pool dimensions to increase due to the occurrence of heat accumulation during the LPBF process. The thinner the wall thickness, the shorter the time to allow for the heat dissipation, cooling, and solidification of the melt pool during the laser scanning. Therefore, compared to thicker samples, the laser track melts the powder with a shorter distance for thin samples, which does not allow enough time for full melt pool solidification before the next laser scan track. In addition, thin samples provide less surface area resulting in less heat dissipation and higher heat accumulation creating larger melt pools. The melt pool dimensions result shows that with increasing thicknesses from 0.5 mm to 0.75 and from 0.5 mm to 1 mm, melt pool width decreases 31% and 45%, respectively. The results did not show any trend of the thin-wall thickness's influence on melt pool depth. It is realized that the thickness of the thin-walls affects melt pool width more effectively in contrast with the melt pool depth dimensions. For instance, by changing the thickness from 0.5 mm to 0.75 mm the melt pool depth is changed by 8%.
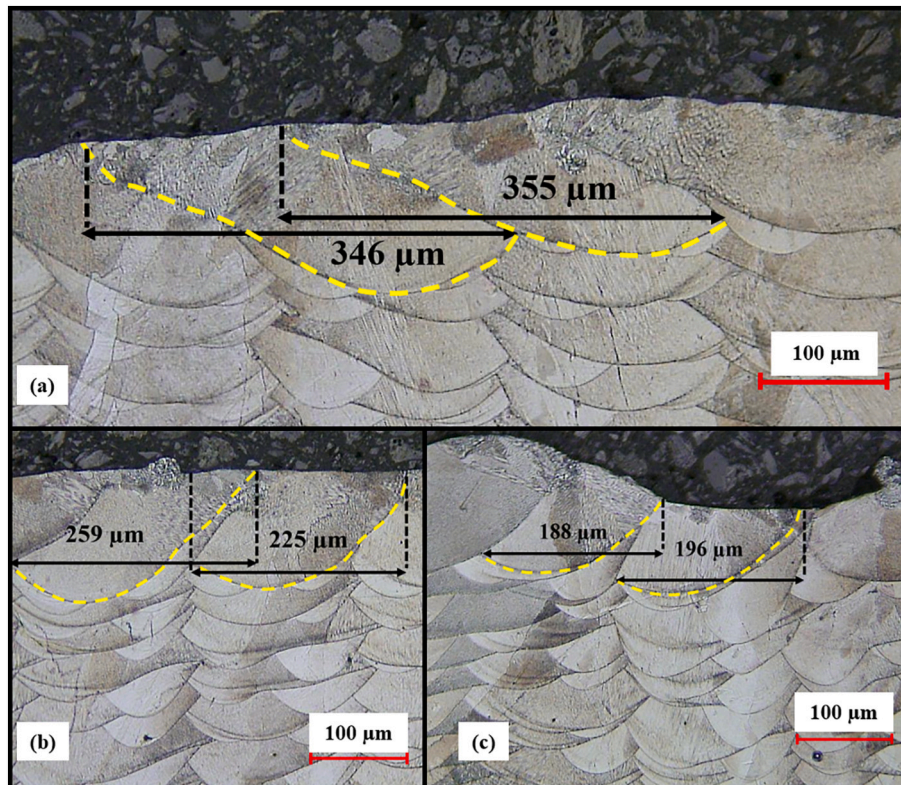

Fig. 9. Melt pool shape and dimensions of thin-walls, a) 0.5 mm thickness, b) 0.75 mm thickness, c) 1 mm thickness.
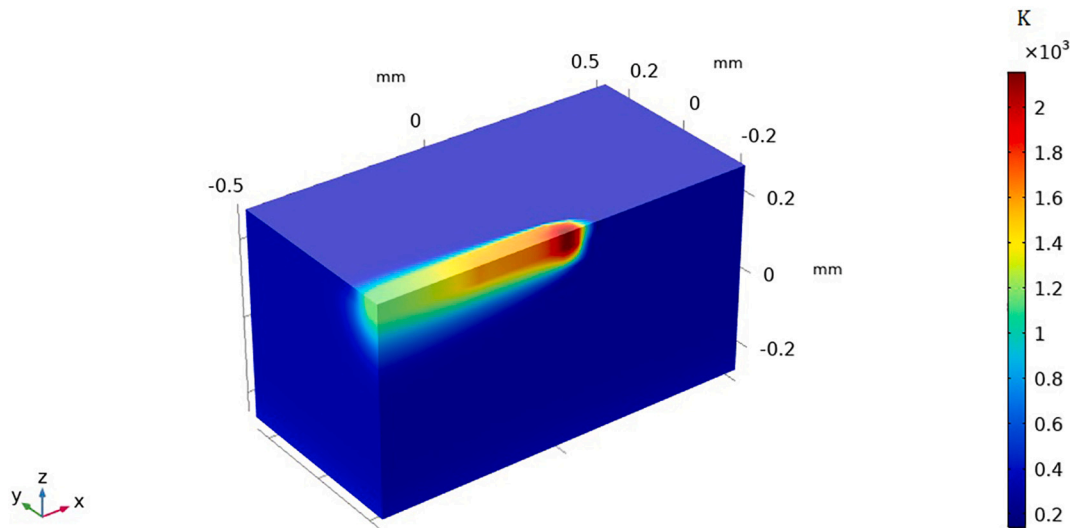
Fig. 10. Schematic of moving laser heat source on a single layer of powder (single-track simulation).
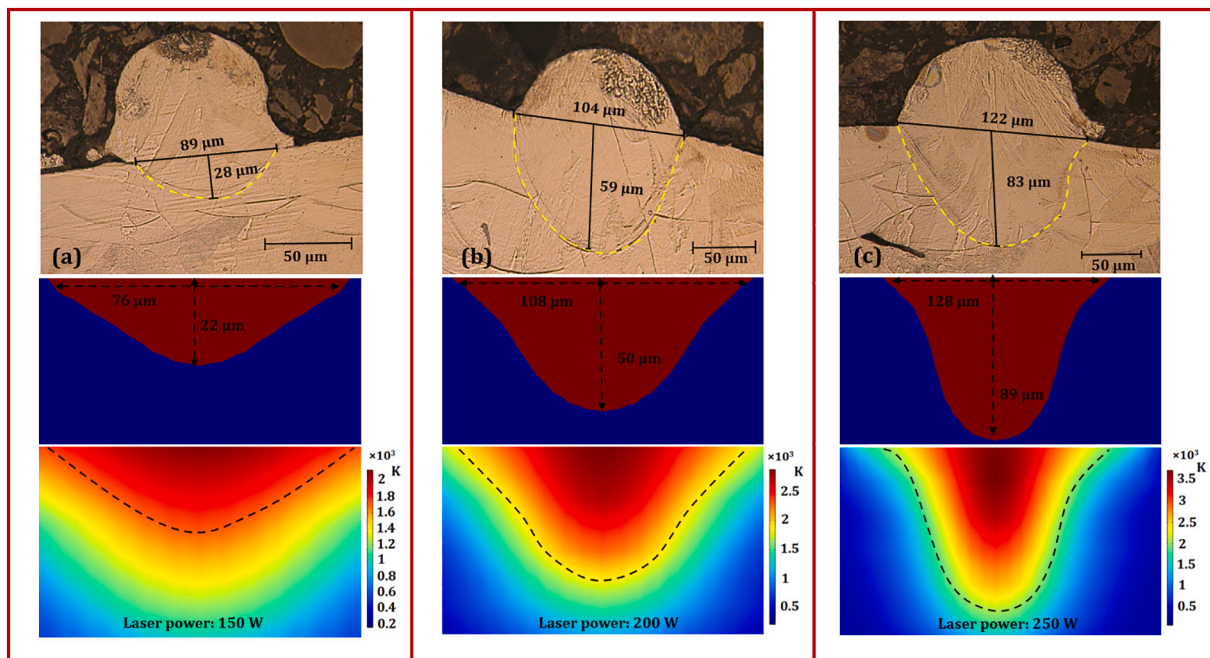

Fig. 11. Single-track melt pool dimensions derived from experimental and numerical results for three different conditions, a) laser power 150 W and scanning speed 1000 mm/s, b) laser power 200 W and scanning speed 1000 mm/s, c) laser power 250 W and scanning speed 1000 mm/s.

4.2. Single-track simulation

A three-dimensional FE model was developed to study the influence of thin-wall thicknesses on the melt pool formation during the building process. It is important to test the numerical model on single-track experimental results to validate the model before predicting thin-wall melt pool dimensions. Calibration of the heat source model is carried out based on single-track experiments at laser powers of 150 W, 200 W, and 250 W and scanning speed of 1000 mm/s. Fig. 10 shows the schematic of the single-track simulation, and Fig. 11 demonstrates the corresponding experimental and numerical results. The melting temperature is shown by the dashed line boundary in the melt pool region derived from simulation results.

The results show that the heat source model was calibrated accurately and, therefore, can predict the effect of part thickness on the melt

pool dimensions. It is important to predict the melt pool dimensions when key process parameters are changing. The calibrated model predicts the width and depth of the melt pool in the various ranges of process parameters. The average percentage difference between calibrated model and experimental results for predicting melt pool width and depth is 14% and 8%, respectively.

On the other hand, experimental results show that melt pool depth and width declined 66% and 27% by reducing the laser power from 250 W to 150 W. Thus, it is observed that laser power has a more dominant effect on melt pool depth compared to melt pool width dimensions [20].

The effect of process parameters (laser power and scanning speed) on melt pool dimensions was investigated to ensure the validity of the developed model. It is observed that increasing the laser power results in delivering higher heat intensity to the material for melting. Consequently, larger melt pool dimensions (melt pool depth and width) are
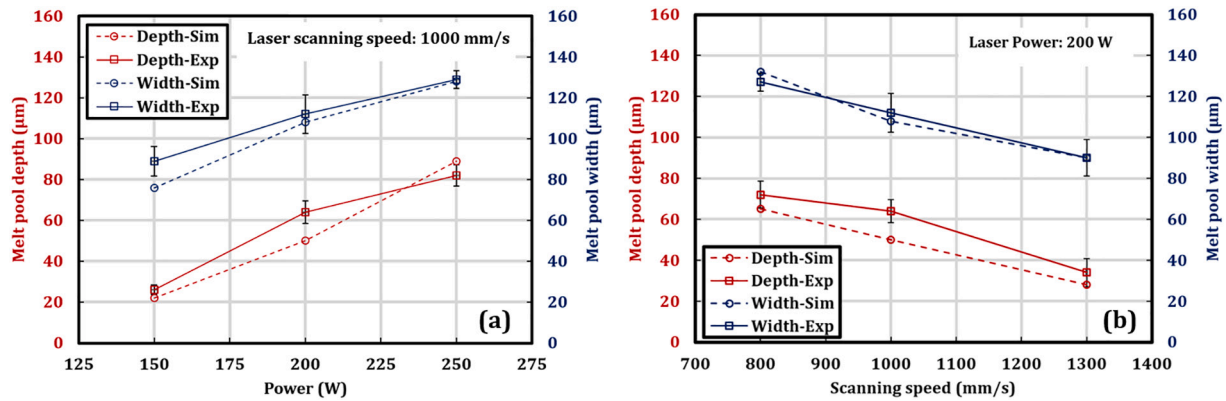
Fig. 12. The influence of process parameters on melt pool dimensions, a) the influence of laser power on melt pool width and depth, b) the influence of scanning speed on melt pool width and depth.
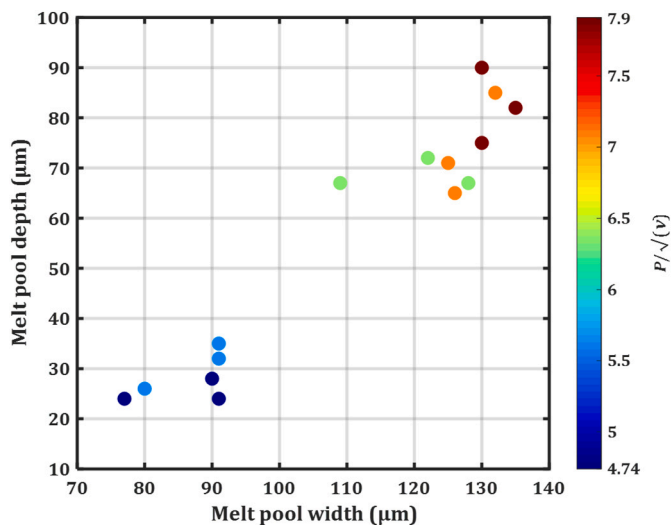

Fig. 13. Melt pool dimensions distribution colored by $P/\sqrt{V}$.

observed. On the other hand, an increase in the laser scanning speed results in smaller melt pools. Fig. 12 illustrates the predicted model versus experimental data and the effect of process parameters on melt pool dimensions. The standard deviation and mean value are indicated on the experimental data point. The average percentage prediction difference between simulation and experimental ones for melt pool depth and width is 16% and 5%, respectively.

Before going to the next section, a brief discussion about a combined process parameter called energy density ($P/\sqrt{V}$) is introduced here, which will be used in Section 4.6 to provide a better understanding of the selection of process parameters versus different thin-wall thicknesses. $P/\sqrt{V}$ has been widely used by other researchers to investigate its effects on melt pool dimensions [20,22,35]. Based on this combined process parameter, Fig. 13 plots the melt pool width versus depth measurements. It is found that melt pool depth and width dimensions are elevated by increasing $P/\sqrt{V}$.

4.3. Multi-track simulation

The calibrated heat source model (Section 4.2) was used for multi-track simulations to study the effect of wall thickness on melt pool dimensions. The multi-track simulations were conducted using the same scanning strategy with the same geometries as those of the experimentally printed thin-walls (Fig. 2). Fig. 14 shows the schematic of the three multi-track simulations with different wall thicknesses. The multi-track

simulation of one layer was carried out by adding 40 μm of Hastelloy X powder on top of the base material followed by laser scanning. Results from Fig. 14 show the temperature distribution in the whole part during the laser scanning. A detailed analysis is given below. It should be noted that to save the computational time only a multi-track simulation of the top layer has been conducted and the results showed that the melt pool dimensions are similar to multi-track multi-layer simulation. Further detail and explanations are described in Fig. S.2 of the supplementary material.

In order to investigate the influence of the wall thickness on melt pool dimensions, the cross-section plane was created perpendicular to the direction of laser movement. The melt pool geometries from the cut-planes were plotted in the center and near the edge of the printed parts to analyze the effect of geometry and wall thickness on melt pool dimensions. The corresponding melt pool regions are shown in Fig. 15a (near the middle of the thin-wall) and Fig. 15b (near the edge of the thin-wall).

Derived melt pools from the edge of the thin-walls show that as multiple tracks of laser scan pass adjacent to each other, the melt pool shapes tend to be elongated due to the heat accumulation. This phenomenon happens because the melt pool does not have enough time to solidify as the laser spot melts the adjacent tracks. It can be clearly seen that the melt pool is drastically elongated for the thin-wall thickness of 0.5 mm. Results show that by decreasing the thickness of the thin-walls from 1 mm to 0.5 mm, the stabilized melt pool width enlarges approximately 1.5 and 2 times in the edge and middle cross-section plane, respectively.

The melt pool geometries derived from two different cut plane sections show that the temperature distribution close to the edge of the geometry domain is higher due to the heat accumulation phenomenon. As a result, the melt pool dimensions extracted from the edge of thin-walls are larger than melt pool dimensions derived from mid-plane cross-sections. For instance, the stabilized melt pool width of thin-wall thicknesses of 0.75 mm and 1 mm for the edge cross-section plane are 1.2 and 1.3 times bigger than the melt pool width derived in the middle domain area, respectively. It can be seen from the results (Fig. 15) that the melt pool dimensions seem to stabilize after a few tracks. Therefore, the first track shows the smallest melt pool and does not reflect the real melt pool dimensions. As the process continues, melt pool dimensions enlarge, and after passing several laser tracks, the melt pools stabilize. Besides, thinner walls take a longer time to reach stabilized melt pools due to larger heat accumulation. Fig. 16a–b shows the quantitative melt pool dimensions for middle and edge planes, respectively. The melt pool evolution results (Fig. 16a) show that the melt pool width for the 0.5 mm, 0.75 mm, and 1 mm wall thickness stabilizes after 10, 8, and 5 laser tracks in the middle section region, respectively. Comparison between the melt pools from the middle and edge of the part shows that melt pool
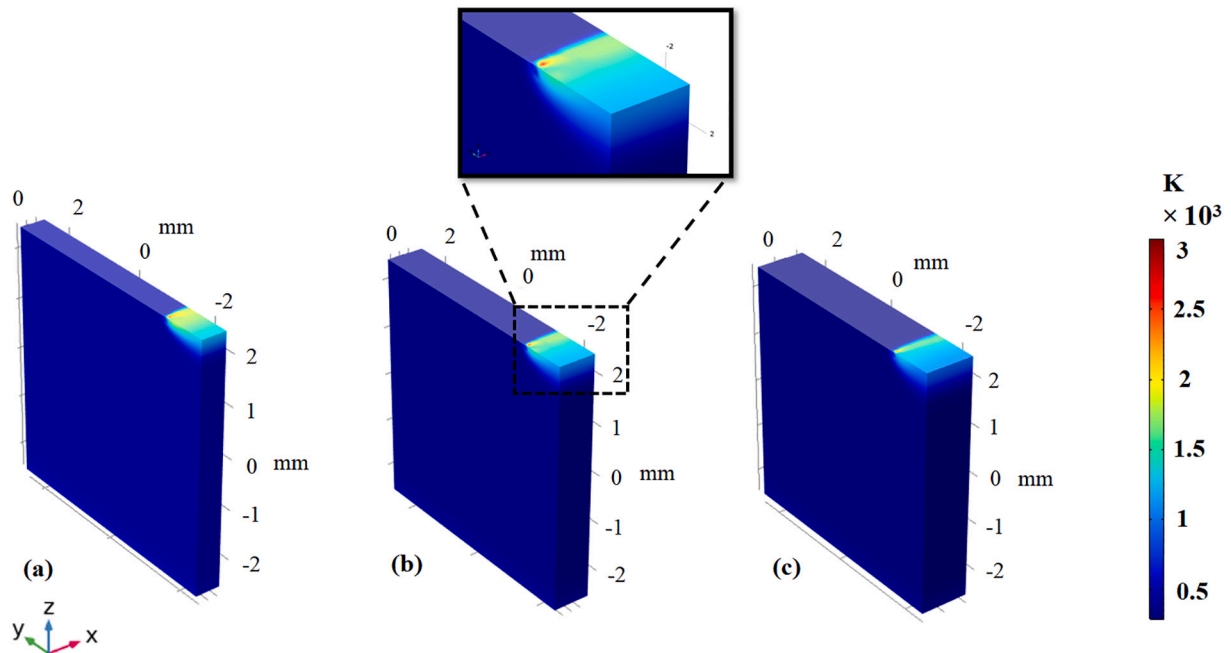
Fig. 14. Multi-track simulation of three different conditions of geometry sizes (5 mm height) with same process parameters, laser power 200 W, scanning speed 1000 mm/s and hatch distance 90 μm, a) thickness 0.5 mm, b) thickness 0.75 mm, c) thickness 1 mm.
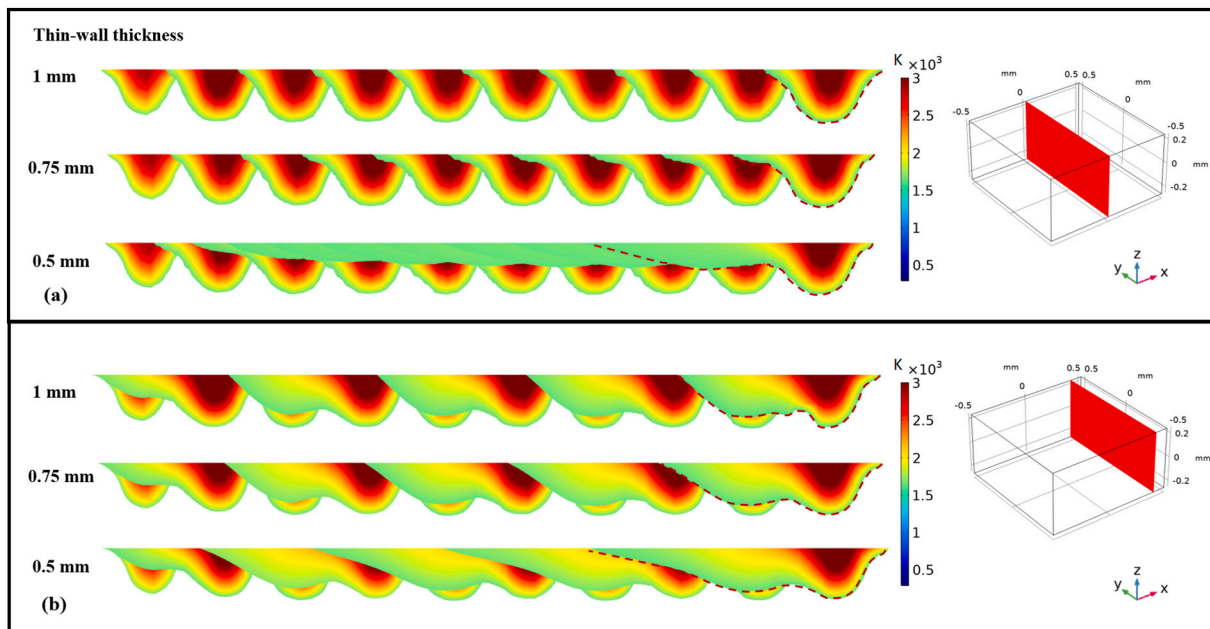

Fig. 15. Melt pool geometries of multi-track simulation, a) melt pools derived from the middle cut plane and, b) the edge of the printed parts for process parameters, laser power 200 W, scanning speed 1000 mm/s and hatch distance 90 μm.

stability is achieved after a larger number of tracks for the edge of the parts (Fig. 16b). The simulation results show that on average, edge melt pools stabilize after 10 tracks.

It should be noted that, based on the observation from experimental results, the melt pool depth does not change significantly. It is realized from the simulation results that a reduction in the thickness from 1 mm to 0.75 mm leads to a 20% increase in stabilized melt pool width while decreasing the thin-wall thicknesses from 0.75 mm to 0.5 mm enlarges the melt pool width to 40% in the middle section region. On the other hand, a decrease in the thickness from 1 mm to 0.75 mm results in a 10% increase in stabilized melt pool width while a reduction in thickness

from 0.75 mm to 0.5 mm leads to an increase of melt pool width by 25% in the edge plane. In addition, the melt pool width dimensions derived from the edge-cross section plane are approximately 20% and 25% larger for thin-wall thicknesses of 0.75 mm and 1 mm, respectively compared with extracted middle-plane melt pool dimensions.

4.4. Validation of simulation results

The simulation results discussed in Section 4.3 were also validated with experimental results to highlight the strength of the proposed model (Fig. 17). The validation results in Fig. 17 show the melt pool
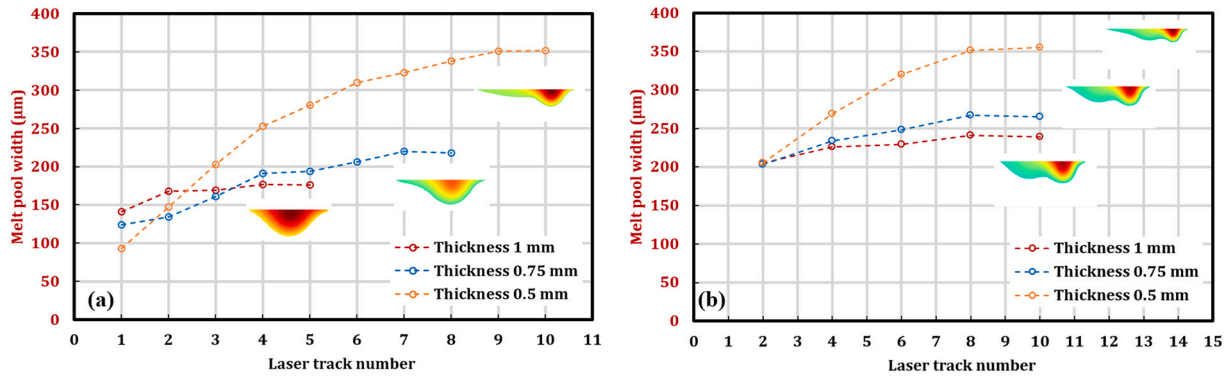
Fig. 16. Melt pool evolution during multi-track LPBF process, a) melt pool derived from the middle plane cross-section, b) melt pool derived from the edge plane cross-section.
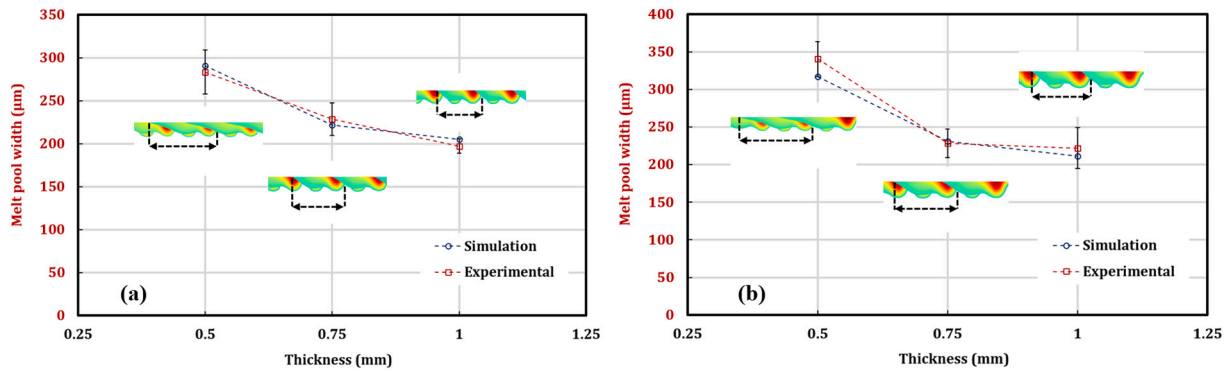

Fig. 17. Validation of multi-track simulation results derived from the edge cross-section plane, a) middle tracks and b) edge tracks melt pool width dimensions.

evolution at the edge cross-section of the thin-walls with different thicknesses. Simulation results show acceptable agreement with experimental ones. It should be noted that all simulation results fall within the error bars from the experimental results. Fig. 17a demonstrates the experimental and simulated melt pool width dimensions in the middle tracks of thin-wall thickness, while the results from the edge tracks of the thin-walls are shown in Fig. 17b. The percentage difference between simulation and mean experimental results for the middle tracks of thin-wall thicknesses of 0.5 mm, 0.75 mm, and 1 mm were found to be 7%,

7%, and 11%, respectively. On the other hand, the percentage difference for the edge tracks of thin-wall thicknesses 0.5 mm, 0.75 mm, and 1 mm were 9%, 7%, and 5%, respectively. It is observed that by increasing the thickness of the thin-walls from 0.5 mm to 1 mm, the melt pool width of middle and edge tracks declined by 30% and 35%, respectively. Besides, the validation results shown in Fig. 17 demonstrate that melt pool width dimensions of the edge tracks of thin-wall thickness 0.5 mm, 0.75 mm, and 1 mm are 17%, 4% and, 11% larger than middle tracks. The melt pool near the edges of the thin-walls has less time to solidify until the
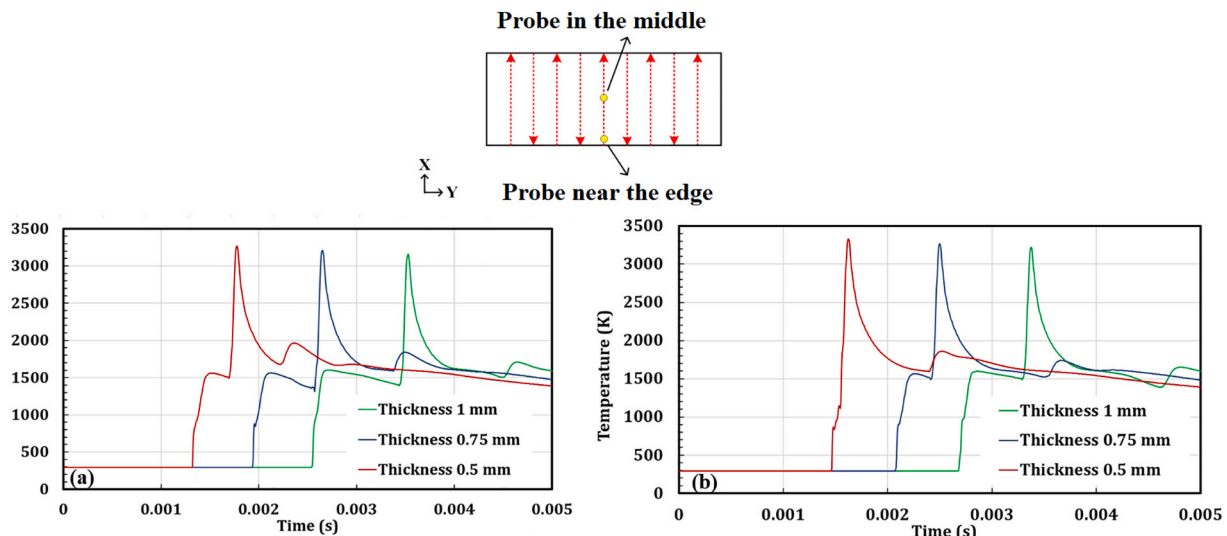

Fig. 18. The transient temperature profile of three thin-wall thicknesses, a) probe in the middle, and b) near the edge of the domain geometry.

next adjacent laser track. As a result, the melt pool width near the edges of the thin-walls is elongated compared to middle tracks.

4.5. Transient temperature profile and temperature gradient

As mentioned in Section 4.3, the reason behind elongated melt pool geometries stems from heat accumulation induced during the LPBF process and an increase in the transient temperature profile of thinner parts. For further investigation on the temperature distribution during the process, two probes on the top surface of the three geometries were located for capturing the transient temperature profile. In order to investigate the influence of the locations on the transient temperature profile, one of the probes was located close to the edge of the domain geometry to observe the differences between the transient temperature profile between the middle and edge of the thin-walls. The schematic of the probes' location in the middle and the edge of the sample's top surface is shown in Fig. 18.

Fig. 18a–b shows the transient temperature profile of three thin-walls with different thicknesses derived from the probe in the middle and the edge of the domain geometry using the same process parameters (laser power 200 W and scanning speed 1000 mm/s), respectively. Transient temperature profile results illustrate that by decreasing the thickness of the parts, peak temperature gradually increases due to the heat accumulation phenomenon.

Table 2 shows that the maximum temperatures derived from the probe in the center of thin-wall geometries with 1 mm, 0.75 mm, and 0.5 mm thicknesses which were found to be 3157 K, 3207 K, and 3265 K, respectively. Similarly, the transient temperatures extracted from the probe near the edge of the thin-wall demonstrate that the peak temperature elevates due to heat accumulation. The maximum temperature derived from the probe in the edge of the thin-wall thicknesses of 1 mm, 0.75 mm, and 0.5 mm are 3221 K, 3268 K, and 3332 K, respectively. The simulation results indicate that by decreasing the thickness of the thin-walls from 1 mm to 0.5 mm the maximum temperature in the center and the edge of the thin-walls increase by 3%. Besides, the maximum temperature near the edge was 2% higher than the center. The reason behind this is that heat dissipation in the middle section area is higher than the edge of the domain part and the laser track near the edge has less time to be cooled down. These results are consistent with the larger melt pool dimensions observed in the edge of the domain geometry in Section 4.3.

To further investigate the effect of the transient temperature profile on the final microstructure of the printed parts, the average temperature gradient was extracted from the simulated geometries. As is shown in Fig. 19, the derived temperature gradient related to the thinnest fabricated parts was higher than other thin-walls. The maximum temperature gradient during the process of the thin-walls with different thicknesses of 1 mm, 0.75 mm, and 0.5 mm was found to be 2.7×10^6 (K/m), 3.1×10^6 (K/m), and 3.9×10^6 (K/m), respectively. Thus, the results indicate that by increasing the thickness of the parts from 0.5 mm to 1 mm the temperature gradient decreased by approximately 30%.

There are numerous studies on the effect of temperature gradient on the microstructure which indicates that temperature gradient has a direct relationship with the cooling rate [36–39]. The following equation (Eq. (17)) indicates the direct relationship between temperature gradient and cooling rates [40]:

Table 2
The maximum temperature relating to different thin-wall thicknesses.

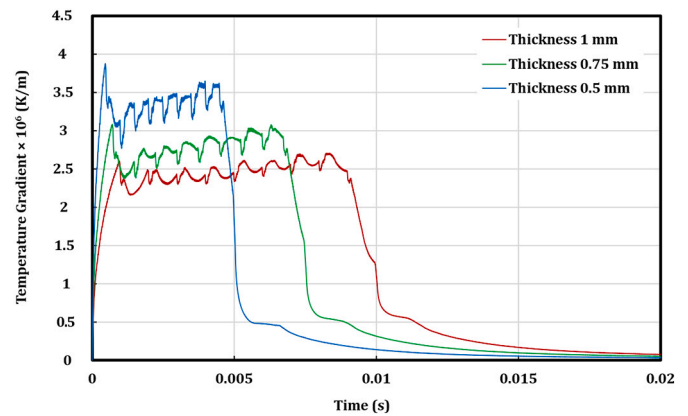| Thin-wall thickness (mm)	Maximum temperature (K)	
	Middle	Edge
0.5	3265	3332
0.75	3207	3268
1	3157	3221

Fig. 19. The extracted average temperature gradient during the LPBF process of different thin-wall thicknesses.

$$\dot{T} = G \times R \tag{17}$$

where $\dot{T}$, G and R are cooling rates, temperature gradient, and solidification rate, respectively.

Since the temperature gradient is directly proportional to the cooling rate, a significant change in the average G value of a deposited layer can influence the average cooling rate of the entire successive layer. It should be noted that the solidification rate may not be changed significantly for various thin-wall thicknesses as it is mainly depending on laser scanning speed during LPBF [41].

Due to repetitive melting of the previously solidified layers in LPBF, most engineering alloys show columnar grain morphology as a result of epitaxial growth. It should be mentioned the directional heat flow condition in LPBF is parallel to building direction (BD) due to the heat sink effect of the substrate. Therefore, the columnar grains are aligned with BD (Fig. 20). Moreover, the nucleation rate during non-equilibrium solidification is a function of undercooling temperature which is being dependent on the processing conditions. The undercooling temperature can provide the extra energy which is required for solid nuclei to form from liquid metal. In a non-equilibrium condition, undercooling temperature varies with cooling rate values. Lower cooling rate values reduce the undercooling temperature and cause lower nucleation densities. Therefore, different temperature gradients, hence, cooling rates due to thickness change could result in variation in the nucleation rate and microstructure, consequently.

To investigate the microstructure variation, an Electron Backscatter Diffraction (EBSD) analysis has been performed to study the effect of the thin-wall thickness. Specifically, inverse pole-figure (IPF) maps were analyzed to comprehend the effect of a transient temperature profile and temperature gradient on the average grain size of printed thin-walls with different thicknesses. Fig. 20 depicts the IPF maps of samples with different thicknesses of 0.5 mm, 0.75 mm, and 1 mm. The results show that the thin-wall with 0.5 mm thickness has a smaller grain size compared to the 1 mm thickness. The average grain size of 216 μm, 198 μm, and 167 μm (Fig. 21) is observed for the thin-wall thickness of 1 mm, 0.75 mm, and 0.5 mm, respectively. Further detail regarding the calculation of the average grain size is described in the supplementary material. The larger grain size can be attributed to the lower temperature gradient and cooling rate induced during the process due to the sample's larger thickness. Thus, a lower undercooling temperature can result to have lower nucleation rate and coarser grain structure when the thicker wall is compared to the thinner wall. Therefore, the simulation results are consistent with experimental observations. A higher peak temperature was observed from thinner parts (Fig. 18). Consequently, the temperature gradient and cooling rate are increased by decreasing the thickness of the parts. Therefore, increasing the cooling rate leads to
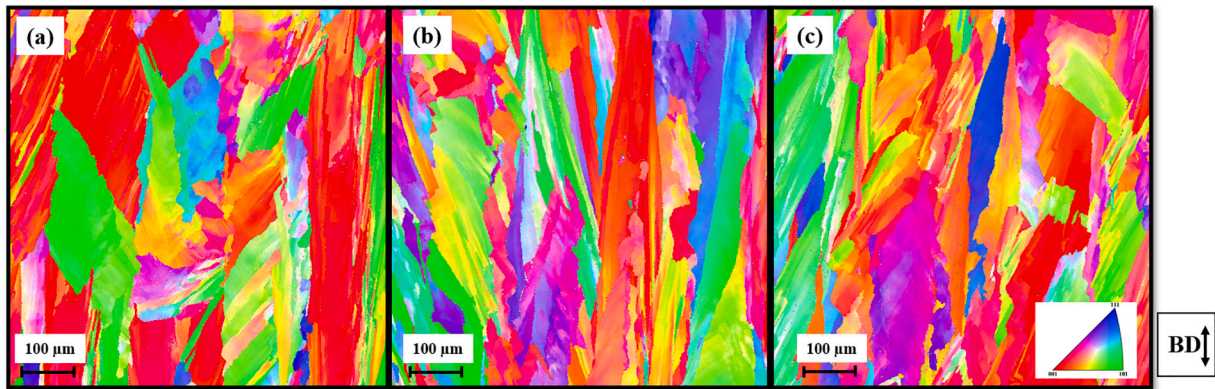
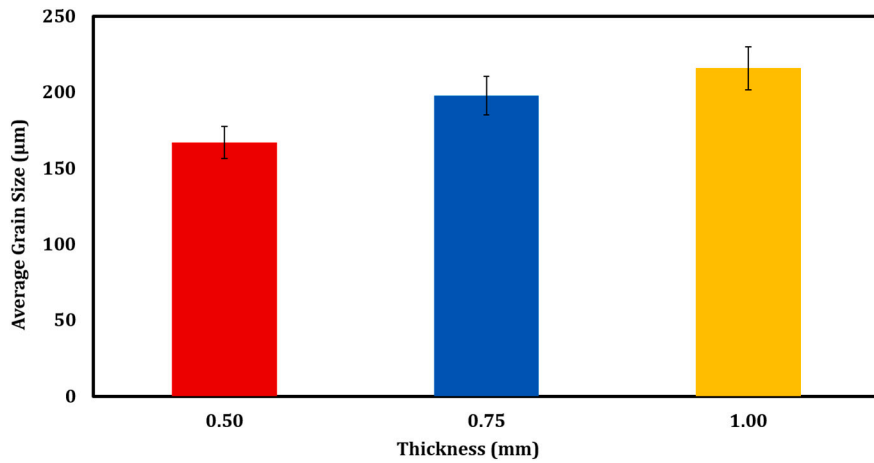**Fig. 20.** EBSD pictures of printed thin-walls with different thicknesses of a) 1 mm, b) 0.75 mm, and c) 0.5 mm.

Fig. 21. The average grain size relating to different printed thin-wall thicknesses.
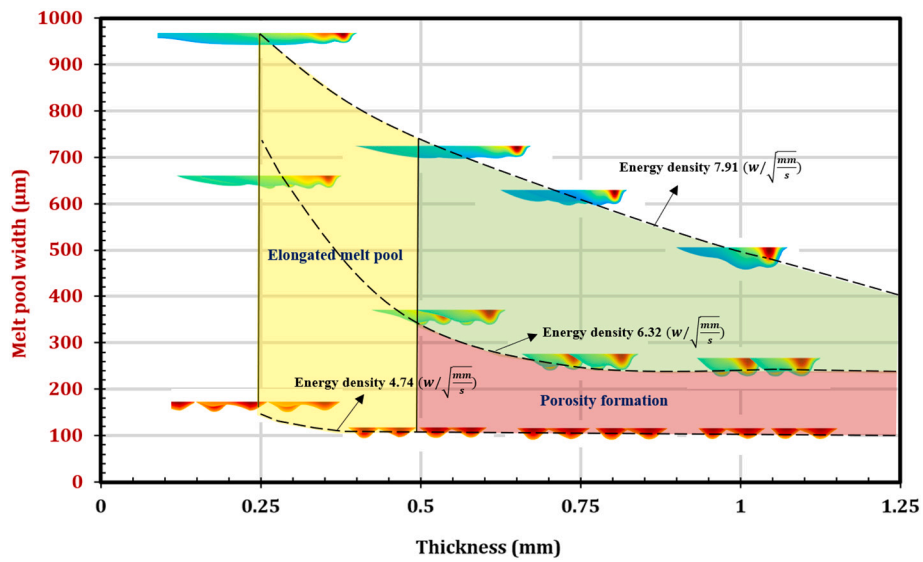

Fig. 22. The process mapping results of melt pool width.

a reduction in the grain size of the manufactured parts by increasing the nucleation rate [39].

4.6. Process mapping

The validation of the single-track and multi-track results highlights the strength of the LPBF model used in this work. Therefore, the model was used to further investigate the effect of thin-walls thickness and process parameters on melt pool dimensions. Melt pool dimensions were derived for various process parameters (Laser power: 150 W, 200 W, and 250 W, Scanning speed: 1000 mm/s) which result in acquiring different $P/\sqrt{V}$. Multi-track simulations were run with varying process parameters and different thin-wall thicknesses. Fig. 22 demonstrates the influence of $P/\sqrt{V}$ and thin-wall thicknesses on the melt pool dimensions. Three different regions based on the geometry of melt pools can be identified. The red color zone shows non-overlapping melt pools for low energy density values which would result in a low density of the part for thicknesses greater than 0.5 mm. However, for thinner walls, the low energy density seems to produce overlapping melt pools which would reduce the porosity. On the other hand, the yellow color zone demonstrates the elongated melt pool shapes due to heat accumulation for thin-wall thicknesses less than 0.5 mm. Generally, elongated melt pools are observed for higher energy density with thinner thin-wall thickness. This larger melt pool width can be detrimental due to inducing higher residual stress of the printed parts [13]. The proper melt pool shapes are represented by the green color region between $P/\sqrt{V}$ range of 6.32 to 7.91 with the thin-wall thicknesses larger than 0.5 mm. Results show that the range of energy density for the various thin-wall thicknesses carries an important relationship between thin-wall thickness and the proper process parameter selection to print high-quality parts.

5. Conclusions

In this study, the effect of thin-wall thickness is investigated on the melt pool geometries and transient temperature during the LPBF process. A three-dimensional (3D) Finite Element (FE) thermal model is developed for simulating the multi-track LPBF process. Both experimental and simulation results are used to investigate the effect of thin-wall thicknesses on melt pool geometries and transient temperature profiles. The following conclusions are drawn based on this study:

1- Experimental results show that for the same process parameters, a reduction in the thickness increases the melt pool dimensions (melt pool width) significantly. The melt pool dimensions result shows that with increasing thicknesses 0.5 mm to 0.75 and 0.5 mm to 1 mm, melt pool width decreases 31% and 45%, respectively. Besides, the results show that the influence of thin-wall thickness on the melt pool width is more dominant than on the melt pool depth.
2- Single-track simulations were validated with experimental results at various laser power range of 150 W to 250 W and scanning speed range of 800 mm/s to 1300 mm/s with an average error of 16% and 5% for melt pool depth and width, respectively. Successful validation of the single-track model enables the model to be further implemented towards multi-track simulation.
3- Thin-wall simulation results show a melt pool evolution during the LPBF process resulting in stabilized melt pools after a few laser tracks have been scanned. It is realized that this is due to the high heat accumulation observed in thin-wall samples. Besides, the melt pool geometries near the edge of the part show higher dimensions of melt pool geometries compared to the middle cross-section.
4- Comparison of the experimental and simulated melt pools of thin-wall geometries have been presented. The percentage difference between simulation and mean experimental results for the middle tracks of thin-wall thicknesses of 0.5 mm, 0.75 mm, and 1 mm were found to be 7%, 7%, and 11%, respectively. On the other hand, the

percentage difference for the edge tracks of thin-wall thicknesses 0.5 mm, 0.75 mm, and 1 mm were 9%, 7%, and 5%, respectively. These results show the strength of the model proposed in this work.
5- The gradual increase in the peak transient temperature profile shows the heat accumulation phenomenon exists during the LPBF process. As a result, by decreasing the thicknesses of the thin-walls from 1 mm to 0.5 mm the peak transient temperature rises 3% approximately. Besides, the maximum temperature in the edge location is 2% higher than the center of thin-walls which is consistent with the larger melt pool dimensions in the edge of the domain geometry. On the other hand, the simulation results show a higher temperature gradient during the process of thinner parts which results in a smaller grain size of the final microstructure.
6- A process parameter map based on the combined parameter $P/\sqrt{V}$ shows that the conduction melt pool zone relies on the energy densities between 6.32 $W/\sqrt{mm/s}$ to 7.91 $W/\sqrt{mm/s}$ for the thin-wall thicknesses larger than 0.5 mm. Elongated melt pools are observed in higher energy density for thin-wall thickness between 0.25 mm and 0.5 mm. Besides, non-overlapping melt pools are created in the red region with a lower energy density and thickness larger than 0.5 mm. As a result, printed parts in this region may have higher porosity and lower mechanical properties. The results highlight the importance of part thickness-based parameter selection.

CRediT authorship contribution statement

Shahriar Imani Shahabad: Conceptualization, Methodology, Software, Validation, Writing - original draft, Writing - review & editing. **Usman Ali**: Formal analysis, Investigation, Writing - review & editing. **Zhidong Zhang**: Investigation, Software, Writing - review & editing. **Ali Keshavarzkermani**: Formal analysis, Writing - review & editing. **Reza Esmaeilizadeh**: Formal analysis, Writing - review & editing. **Ali Bonakdar**: Project administration, Supervision, Writing - review & editing. **Ehsan Toyserkani**: Supervision, Funding acquisition, Resources, Writing - review & editing.

Declaration of competing interest

The authors declare that they have no known competing financial interests or personal relationships that could have appeared to influence the work reported in this paper.

Acknowledgment

Appendix A. Supplementary data

Supplementary data to this article can be found online at https://doi.org/10.1016/j.jmapro.2022.01.029.

References

[1] Du Y, You X, Qiao F, Guo L, Liu Z. A model for predicting the temperature field during selective laser melting. Results Phys 2019;12:52–60. https://doi.org/10.1016/j.rinp.2018.11.031.
[2] Bayat M, Mohanty S, Hattel JH. A systematic investigation of the effects of process parameters on heat and fluid flow and metallurgical conditions during laser-based

powder bed fusion of Ti6Al4V alloy. Int J Heat Mass Transf 2019;139:213–30. https://doi.org/10.1016/j.ijheatmasstransfer.2019.05.017.

[3] Fayazfar H, Salarian M, Rogalsky A, Sarker D, Russo P, Paserin V, et al. A critical review of powder-based additive manufacturing of ferrous alloys: process parameters, microstructure and mechanical properties. Mater Des 2018;144: 98–128. https://doi.org/10.1016/j.matdes.2018.02.018.

[4] Yavari R, Williams R, Riensche A, Hooper PA, Cole KD, Jacquemetton L, et al. Thermal modeling in metal additive manufacturing using graph theory – application to laser powder bed fusion of a large volume impeller. Addit Manuf 2021;41:101956. https://doi.org/10.1016/j.addma.2021.101956.

[5] Mahmoodkhani Y, Ali U, Liravi F, Esmaeilizadeh R, Marzbanrad E, Bonakdar A, et al. An effective statistical approach to determine the most contributing process parameters on the surface roughness quality of hastelloy X components made by laser powder-bed fusion. In: Int. Congr. Appl. Lasers Electro-Optics. 2018. Laser Institute of America; 2018. P115.

[6] Zhang Z, Ali U, Mahmoodkhani Y, Huang Y, Shahabad SI, Kasinathan AR, et al. Experimental and numerical investigation on the effect of layer thickness during laser powder-bed fusion of stainless steel 17–4PH. Int J Rapid Manuf 2020;9:212. https://doi.org/10.1504/ijrapidm.2020.107735.

[7] Bai Y, Yang Y, Xiao Z, Zhang M, Wang D. Process optimization and mechanical property evolution of AlSiMg0.75 by selective laser melting. Mater Des 2017. https://doi.org/10.1016/j.matdes.2017.11.045.

[8] Gunenthiram V, Peyre P, Schneider M, Dal M, Coste F, Fabbro R. Analysis of laser–melt pool–powder bed interaction during the selective laser melting of a stainless steel. J Laser Appl 2017;29:022303. https://doi.org/10.2351/1.4983259.

[9] Thijs L, Verhaeghe F, Craeghs T, Van Humbeeck J, Kruth JP. A study of the microstructural evolution during selective laser melting of ti-6Al-4V. Acta Mater 2010;58:3303–12. https://doi.org/10.1016/j.actamat.2010.02.004.

[10] Chen Q, Guillemot G, Gandin CA, Bellet M. Three-dimensional finite element thermomechanical modeling of additive manufacturing by selective laser melting for ceramic materials. Addit Manuf 2017;16:124–37. https://doi.org/10.1016/j.addma.2017.02.005.

[11] Siao YH, Da Wen C. Thermal analysis of anisotropic heat conduction model with experimental validation on molten pool during selective laser melting. Mater Today Commun 2021;27:102425. https://doi.org/10.1016/j.mtcomm.2021.102425.

[12] Keshavarzkermani A, Marzbanrad E, Esmaeilizadeh R, Mahmoodkhani Y, Ali U, Enrique PD, et al. An investigation into the effect of process parameters on melt pool geometry, cell spacing, and grain refinement during laser powder bed fusion. Opt Laser Technol 2019;116:83–91. https://doi.org/10.1016/j.optlastec.2019.03.012.

[13] Staub A, Spierings AB, Wegener K. Correlation of meltpool characteristics and residual stresses at high laser intensity for metal lpbf process. Adv Mater Process Technol 2019;5:153–61. https://doi.org/10.1080/2374068X.2018.1535643.

[14] Criales LE, Arsoy YM, Lane B, Moylan S, Donmez A, Özel T. Laser powder bed fusion of nickel alloy 625: experimental investigations of effects of process parameters on melt pool size and shape with spatter analysis. Int J Mach Tool Manuf 2017;121:22–36. https://doi.org/10.1016/j.ijmachtools.2017.03.004.

[15] Kamath C. Data mining and statistical inference in selective laser melting. Int J Adv Manuf Technol 2016;86:1659–77. https://doi.org/10.1007/s00170-015-8289-2.

[16] Li Z, Yang S, Liu B, Liu W, Kuai Z, Nie Y. Simulation of temperature field and stress field of selective laser melting of multi-layer metal powder. Opt Laser Technol 2021:140. https://doi.org/10.1016/j.optlastec.2020.106782.

[17] Jin P, Tang Q, Song J, Feng Q, Guo F, Fan X, et al. Numerical investigation of the mechanism of interfacial dynamics of the melt pool and defects during laser powder bed fusion. Opt Laser Technol 2021;143:107289. https://doi.org/10.1016/j.optlastec.2021.107289.

[18] Soundararajan B, Sofia D, Barletta D, Poletto M. Review on modeling techniques for powder bed fusion processes based on physical principles. Addit Manuf 2021; 47:102336. https://doi.org/10.1016/j.addma.2021.102336.

[19] Yuan W, Chen H, Cheng T, Wei Q. Effects of laser scanning speeds on different states of the molten pool during selective laser melting: simulation and experiment. Mater Des 2020;189:108542. https://doi.org/10.1016/j.matdes.2020.108542.

[20] Shahabad SI, Zhang Z, Keshavarzkermani A, Ali U, Mahmoodkhani Y, Esmaeilizadeh R, et al. Heat source model calibration for thermal analysis of laser powder-bed fusion. Int J Adv Manuf Technol 2020;106:3367–79. https://doi.org/10.1007/s00170-019-04908-3.

[21] Li J, Wei Z, Yang L, Zhou B, Wu Y, Chen S-G, et al. Finite element analysis of thermal behavior and experimental investigation of Ti6Al4V in selective laser melting. Optik (Stuttg) 2019:163760. https://doi.org/10.1016/j.ijleo.2019.163760.

[22] Zhang Z, Huang Y, Rani Kasinathan A, Imani Shahabad S, Ali U, Mahmoodkhani Y, et al. 3-dimensional heat transfer modeling for laser powder-bed fusion additive manufacturing with volumetric heat sources based on varied thermal conductivity and absorptivity. Opt Laser Technol 2019;109:297–312. https://doi.org/10.1016/j.optlastec.2018.08.012.

[23] Loh LE, Liu ZH, Zhang DQ, Mapar M, Sing SL, Chua CK, et al. Selective laser melting of aluminium alloy using a uniform beam profile. Virtual Phys Prototyp 2014;9:11–6. https://doi.org/10.1080/17452759.2013.869608.

[24] Leicht A, Klement U, Hryha E. Effect of build geometry on the microstructural development of 316L parts produced by additive manufacturing. Mater Charact 2018;143:137–43. https://doi.org/10.1016/j.matchar.2018.04.040.

[25] Liang H, Xie D, Mao Y, Shi J, Wang C, Shen L, et al. The size effect on forming quality of Ti–6Al–4V solid struts fabricated via laser powder bed fusion. Metals (Basel) 2019;9. https://doi.org/10.3390/met9040416.

[26] Piazza S, Merrigan B, Dowling DP, Celikin M. The effects of geometry and laser power on the porosity and melt pool formation in additively manufactured 316L stainless steel. Int J Adv Manuf Technol 2020;111:1457–70. https://doi.org/10.1007/s00170-020-06196-8.

[27] Esmaeilizadeh R, Ali U, Keshavarzkermani A, Mahmoodkhani Y, Marzbanrad E, Toyserkani E. On the effect of spatter particles distribution on the quality of hastelloy X parts made by laser powder-bed fusion additive manufacturing. J Manuf Process 2019;37:11–20. https://doi.org/10.1016/j.jmapro.2018.11.012.

[28] EOS GmbH. Electro optical systems. Material data sheet EOS NickelAlloy HX material data sheet technical data49; 2015.

[29] Sih SS, Barlow JW. The prediction of the emissivity and thermal conductivity of powder beds. Part Sci Technol 2004;22:427–40. https://doi.org/10.1080/02726350490501682.

[30] Ali U, Mahmoodkhani Y, Imani Shahabad S, Esmaeilizadeh R, Liravi F, Sheydaeian E, et al. On the measurement of relative powder-bed compaction density in powder-bed additive manufacturing processes. Mater Des 2018;155: 495–501. https://doi.org/10.1016/j.matdes.2018.06.030.

[31] Promoppatum P, Yao SC, Pistorius PC, Rollett AD. A comprehensive comparison of the analytical and numerical prediction of the thermal history and solidification microstructure of Inconel 718 products made by laser powder-bed fusion. Engineering 2017;3:685–94. https://doi.org/10.1016/J.ENG.2017.05.023.

[32] Kamara AM, Wang W, Marimuthu S, Li L. Modelling of the melt pool geometry in the laser deposition of nickel alloys using the anisotropic enhanced thermal conductivity approach. Proc Inst Mech Eng Part B J Eng Manuf 2011;225:87–99. https://doi.org/10.1177/09544054IEM2129.

[33] Khan MS, Shahabad SI, Yavuz M, Duley WW, Biro E, Zhou Y. Numerical modelling and experimental validation of the effect of laser beam defocusing on process optimization during fiber laser welding of automotive press-hardened steels. J Manuf Process 2021;67:535–44. https://doi.org/10.1016/j.jmapro.2021.05.006.

[34] Shahabad SI, Karimi G, Toyserkani E. An extended Rosenthal ' s model for laser powder-bed fusion additive manufacturing: energy auditing of thermal boundary conditions. Lasers Manuf Mater Process 2021:1–24.

[35] Rubenchik AM, King WE, Wu SS. Scaling laws for the additive manufacturing. J Mater Process Technol 2018;257:234–43. https://doi.org/10.1016/j.jmatprotec.2018.02.034.

[36] Köhnen P, Ewald S, Schleifenbaum JH, Belyakov A, Haase C. Controlling microstructure and mechanical properties of additively manufactured high-strength steels by tailored solidification. Addit Manuf 2020;35:101389. https://doi.org/10.1016/j.addma.2020.101389.

[37] Esmaeilizadeh R, Keshavarzkermani A, Ali U, Behravesh B, Bonakdar A, Jahed H, et al. On the effect of laser powder-bed fusion process parameters on quasi-static and fatigue behaviour of hastelloy X: a microstructure/defect interaction study. Addit Manuf 2021;38:101805. https://doi.org/10.1016/j.addma.2020.101805.

[38] Keshavarzkermani A, Esmaeilizadeh R, Enrique PD, Asgari H, Zhou NY, Bonakdar A, et al. Static recrystallization impact on grain structure and mechanical properties of heat-treated hastelloy X produced by laser powder-bed fusion. Mater Charact 2021;173:110969. https://doi.org/10.1016/j.matchar.2021.110969.

[39] Qin H, Fallah V, Dong Q, Brochu M, Daymond MR, Gallerneault M. Solidification pattern, microstructure and texture development in laser powder bed fusion (LPBF) of Al10SiMg alloy. Mater Charact 2018;145:29–38. https://doi.org/10.1016/j.matchar.2018.08.025.

[40] Liu S, Zhu H, Peng G, Yin J, Zeng X. Microstructure prediction of selective laser melting AlSi10Mg using finite element analysis. Mater Des 2018;142:319–28. https://doi.org/10.1016/j.matdes.2018.01.022.

[41] Harrison NJ, Todd I, Mumtaz K. Reduction of micro-cracking in nickel superalloys processed by selective laser melting: a fundamental alloy design approach. Acta Mater 2015;94:59–68. https://doi.org/10.1016/j.actamat.2015.04.035.